Journal of Zhejiang University-SCIENCE A (Applied Physics & Engineering) 2024 25(12):1018-1036
www.jzus.zju.edu.cn; www.springer.com/journal/11582
E-mail: jzus_a@zju.edu.cn

Research Article

https://doi.org/10.1631/jzus.A2300516

Permeability of structured porous media: numerical simulations and microfluidic models

Shaokai NIE[1,2,3], Pengfei LIU[1,2,3], Kexin CHEN[1,2,3], Wenyuan WANG[1,2,3], Yunmin CHEN[1,2,3], Bate BATE[1,2,3]✉

[1]*Institute of Geotechnical Engineering, College of Civil Engineering and Architecture, Zhejiang University, Hangzhou 310058, China*
[2]*Hypergravity Research Center, College of Civil Engineering and Architecture, Zhejiang University, Hangzhou 310058, China*
[3]*MOE Key Laboratory of Soft Soils and Geoenvironmental Engineering, Zhejiang University, Hangzhou 310058, China*

Abstract: In this study, the permeability of structured porous media with the microfluidic model is experimentally and numerically determined, and compared with the classic Kozeny-Carman (KC) equation. The Reynolds number (*Re*) varies from 0.83 to 142.98. It is observed that the threshold of the Reynolds number is 1. When *Re* is below the threshold, the permeability is independent of the Reynolds number. When *Re* is over this threshold, the viscous force plays a dominant role and the permeability decreases with the Reynolds number increment. The permeability also rises with the diameter increment. With the same micropillar diameter, the microfluidic model with a triangular pillar arrangement yields 4.5%–7.4% lower permeability than that with a square pillar arrangement. The tortuosity obtained by numerical simulation in the triangular-arrangement model is 5.1%–7.9% higher than that in the square-arrangement model. Based on the arrangement of micropillars, a tortuosity model is proposed for quasi-two-dimensional microfluidic models. There is an inverse relationship between permeability and tortuosity. In addition, the permeability generated by numerical simulation is consistent with that obtained experimentally. However, the permeability estimated by the classic KC equation roughly agrees with experimental results when the porosity is between 0.50 and 0.60. A model proposed in this study is suitable for predicting the permeability of microfluidic models. Furthermore, anisotropy induced by the tilt angle (0°–90°) of a model rectangular micropillar arrangement causes preferential flow and decreases the effective porosity. When the tilt angle increases from 0° to 90°, the tortuosity declines from 2.04 to 1.03, causing the permeability to rise from 1.0×10^{-11} to 4.3×10^{-11} m^2.

Key words: Permeability; Microfluidic model; Porosity; Tortuosity; Anisotropy

1 Introduction

In recent years, porous media characterization has engendered a great deal of interest, due to issues associated with gas and oil production in shale and hydrate (Lefebvre et al., 2008; Cai et al., 2012; Kawagoe et al., 2016; De et al., 2018), as well as applications in chemical engineering (Rickenbach et al., 2014), fuel cells (Kumar and Reddy, 2003; Tawfik et al., 2007; Yang et al., 2017), microelectronics cooling (Lu et al., 1998), and biomedicine (Zhang, 2011). The most significant properties of porous media that affect the permeability and fluid transport phenomena, are porosity, pore interconnectivity, pore radius, tortuosity, and specific surface area (Carman, 1939; Cai et al., 2012; Straughan and Harfash, 2013; Lu et al., 2023). It is important to understand the effect of these properties on the characteristics of fluid flow through porous media.

One of the most commonly measured properties, permeability, characterizes the difficulty of flow through porous media, and represents the pore interconnectivity for fluid conductivity (Collins, 1961). Measurement methods include indirect prediction and image analysis from experiments (Lock et al., 2002), as well as techniques involving nuclear magnetic resonance spectroscopy and scanning electron microscopy (Cardona and Santamarina, 2020). The Darcy law is known to be the most common experimental method for determining permeability:

✉ Bate BATE, batebate@zju.edu.cn
Shaokai NIE, https://orcid.org/0000-0002-0887-0241
Bate BATE, https://orcid.org/0000-0002-8692-8402

Received Oct. 11, 2023; Revision accepted Feb. 22, 2024;
Crosschecked Nov. 18, 2024

$$-\frac{\mathrm{d}p}{\mathrm{d}x}=\frac{\mu}{K}U, \tag{1}$$

where $\frac{\mathrm{d}p}{\mathrm{d}x}$ is the hydraulic gradient, μ is the dynamic viscosity of the fluid, U is the average pore velocity, and K is the intrinsic permeability of the porous medium. This relation is only applicable to viscous-dominated flows (Loosveldt et al., 2002; Liu and Tran, 2018). For $Re>1$, the relationship becomes nonlinear and a modified Darcy equation called Forchheimer law has been proposed (Lee and Yang, 1997):

$$-\frac{\mathrm{d}p}{\mathrm{d}x}=\frac{\mu}{K}U+\delta\rho U^2, \tag{2}$$

where δ is the inertial resistance coefficient related to the pore shape, pore size, and porosity, and ρ is the fluid density. This is also known as the non-Darcy coefficient.

The major fields connected to microfluidics are molecular analysis, biodefence, molecular biology, and microelectronics (Tamayol and Bahrami, 2011a). With advances in microfluidics and microfabrication techniques, flow through microfluidic model in describing the porous media has become an area of great interest (Wan and Wilson, 1994; Bazylak et al., 2008), such as flow rate and interface wettability impacts on immiscible displacement (Conn et al., 2014; Hu et al., 2018; Chen et al., 2023), fines migration, and pore clogging (Pozrikidis, 1994; Auset and Keller, 2004; Cao et al., 2019; Yang J et al., 2019, 2020a, 2020b; Yin et al., 2023), as shown in Fig. 1. There is no doubt that using a microfluidic model to study permeability of porous media shows great potential. Therefore, many papers have reported the estimation of permeability using the creeping flow of liquids in microchannels with integrated micropillars. The micropillars provide the solid structure in a microfluidic model, which represents the soil skeleton (formation matrix). The diameter of integrated micropillars usually ranges from 20 to 450 μm (Tamayol and Bahrami, 2011b; Tamayol et al., 2012a; Gunda et al., 2013; Liu and Tran, 2018). Gunda et al. (2013) investigated single-phase fluid flow through microchannels with integrated micropillars to calculate the pressure drop and flow resistance. The microchannels contained micropillars arranged in square and staggered formations. Chen (2021) also studied the permeability of a microfluidic model with seepage experiments. Chips with micropillars in a triangular arrangement showed higher pressure drops than those with micropillars in a square arrangement.

Numerical simulation plays an important role in the study of the porous media seepage mechanism at the micrometer scale. There are several numerical methods, such as the computational fluid dynamics (CFD) (Tamayol and Bahrami, 2011c; Tamayol et al., 2012b; Huang et al., 2020), the lattice Boltzmann method (LBM) (Zhou et al., 2022), and the pore network model (PNM) (Raeesi and Piri, 2009). Tamayol et al. (2012b) fabricated several microfluidic samples to investigate the accuracy of a theoretical model compared with experimental and numerical data. Microfluidic samples were fabricated with porosities in the range of 0.35 to 0.95, fiber diameters varying from 50 to 400 μm, and a channel depth of approximately 100 μm. Huang et al. (2020) developed a numerical model of laminar flow in porous media, with square particles. The Reynolds number, streamline, porosity, tortuosity, and fractal dimension were evaluated. Compared to other numerical methods, though the CFD method requires higher computational resources, it has fewer model parameters and does not require calibration.

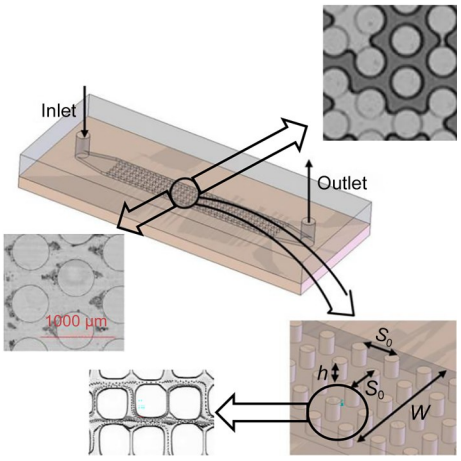

Fig. 1 Schematic illustration of a microfluidic model and its application for permeability, fines migration, and multiphase displacement (Auset and Keller, 2004; Tamayol et al., 2012a; Bate et al., 2022; Chen et al., 2023). h is the height of the micropillar; S_0 is the distance between two neighboring micropillars; W is the width of the channel

However, studies of permeability that are relevant to the geotechnical engineering community and are carried out at the microscale level with a microfluidic model in porous structures are limited. For example,

there are deviations when measuring microchannel flow pressure drop to estimate the permeability of porous media, due to pressure loss at the inlet and outlet ports of the microchannel (Akbari et al., 2009; Nie et al., 2023). The flow condition in a microfluidic model seems to be limited to Darcy flow or creeping flow with low Reynolds numbers (Tamayol et al., 2012a; Gunda et al., 2013). The wall effect is a non-uniform variation of porosity near the wall in porous media, and is neglected in low Reynolds numbers (Castillo-Araiza and Lopez-Isunza, 2008; Chen et al., 2021). Moreover, it has been shown that the pressure drop obtained at the microscale cannot be predicted adequately by large-scale correlations (Koşar et al., 2005; Yazdchi et al., 2011). The existing theoretical models fail to predict the permeability of the microfluidic model accurately (Serrenho and Miguel, 2009; Gunda et al., 2013; Wagner, et al., 2021). Few studies have investigated the influence of microchannels with large particle diameters and moderate Reynolds numbers on the permeability of microfluidic models.

The goal of this study was to assess complementary fluid flow to estimate the permeability of microfluidic models. These particular models have square or staggered arrangements of circular or rectangular micropillars when the experimental Reynolds number varies between 0.83 and 142.98. The effects of Reynolds number, anisotropy, tortuosity, and porosity on permeability are discussed. We also discuss the effect of microchannel depth on permeability. In addition, an analytical tortuosity model based on the 2D rectangular or circular micropillar is proposed. The experimental results are compared with those obtained by numerical simulation and the prediction model proposed in this study. We investigate the applicability of the Kozeny-Carman (KC) equation for the microfluidic model, and analyze the fluid flow streamline in the model via a microscale particle-image velocimetry (μPIV) experiment.

2 Theoretical background

2.1 Reynolds number for microfluidic model flow

Dybbs and Edwards (1984) studied the microscopic fluid dynamics of dye fluid flowing through hexagonally packed spheres, and proposed the Reynolds number:

$$Re=\frac{\rho U D_{\mathrm{h}}}{\mu}, \tag{3}$$

where D_{h} is the average characteristic length scale for the pores. For obstacles like fibers or particles, D_{h} can be re-written as:

$$D_{\mathrm{h}}=\frac{4\varepsilon}{(1-\varepsilon)a_{\mathrm{v}}}, \tag{4}$$

where $a_{\mathrm{v}}=\frac{6}{d}$, d is the particle diameter, and ε is the porosity. The experimental Reynolds numbers here varied between 0.83 and 142.98.

Four flow regimes are defined based on this Reynolds number (Dybbs and Edwards, 1984): (1) $Re<1$, creeping-flow regime; (2) $1\leqslant Re<150$, inertial-flow regime; (3) $150\leqslant Re<300$, unsteady laminar-flow regime; (4) $Re\geqslant 300$, unsteady- and chaotic-flow regime.

2.2 Kozeny-Carman equation and tortuosity

The well-known empirical approach for predicting the permeability of porous media is expressed by the KC equation (Carman, 1956):

$$K=k\left(\frac{\mu}{\gamma_{\mathrm{p}}}\right)=\frac{1}{C_{\mathrm{KC}}S^2}\frac{\varepsilon^3}{(1-\varepsilon)^2}=\frac{1}{C_0\tau^2S^2}\frac{\varepsilon^3}{(1-\varepsilon)^2}, \tag{5}$$

where K is the intrinsic permeability (m^2), k is the permeability coefficient (m/s), γ_{p} is the fluid bulk density, C_{KC} is the KC constant, and S is the specific surface area. The value of C_{KC} depends on factors including the tortuosity τ and the shape of grains C_0 (Wagner et al., 2021). τ is defined as follows (Carman, 1956):

$$\tau=\frac{L_{\mathrm{e}}}{L}, \tag{6}$$

where L_{e} is the length of the streamlines, and L is the sample length.

Tortuosity is related to the pore size, particle shape, and porosity of porous media, in addition to other factors. Various empirical expressions are presented in Table 1 to describe this. Tortuosity models have been obtained by considering particle size and shape (Comiti and Renaud, 1989; Koponen et al., 1996; Wang, 2014), 2D particle arrangement (Yu and Li, 2004; Lanfrey et al., 2010), and the topological

Table 1 Expressions of tortuosity τ

Reference	Equation	Note
Comiti and Renaud (1989)	$\tau=1-P\ln(\varepsilon)$	P is a fitting coefficient and is 0.63 for cubic particles and 0.41 for spherical particles
Koponen et al. (1996)	$\tau=1+0.8(1-\varepsilon)$	Fluid flowed through freely arranged square particles
Yu and Li (2004)	$\tau=\frac{1}{2}\left[1+\frac{1}{2}\sqrt{1-\varepsilon}+\sqrt{1-\varepsilon}\frac{\sqrt{\left(\frac{1}{\sqrt{1-\varepsilon}}-1\right)^2+\frac{1}{4}}}{1-\sqrt{1-\varepsilon}}\right]$	Assuming 2D square particles in an equilateral-triangle arrangement
Feranie and Latief (2013)	$\tau=-0.7145\varepsilon+1.6571$	Proposing a 2D fractal model of porous substance constructed by randomized Sierspinski carpets
Wang (2014)	$\tau=-0.42\varepsilon+1.35$	Simulating the fluid flow in intervals of dense spheres by LBM
Khabbazi et al. (2015)	$\tau=\left(1-\frac{4}{\pi}\right)\varepsilon+\frac{4}{\pi}$	Relationship between tortuosity and porosity within fractal geometries of Sierpinski carpet
Zhang et al. (2020)	$\tau=\frac{3}{8}\left\{\sqrt{\left[1-\sqrt{(1-\varepsilon)m}\right]^2+\tan^2\left[(1-\varepsilon)^{\frac{1}{3}}\theta\right]}+\sqrt{\frac{\tan^2\left[(1-\varepsilon)^{1/3}\theta\right]}{\left[1-\sqrt{(1-\varepsilon)m}\right]^2}}\right\}+\frac{2-\sqrt{(1-\varepsilon)m}}{8\cos\left[(1-\varepsilon)^{1/3}\theta\right]}+\frac{\sqrt{(1-\varepsilon)m}}{8\left[1-\sqrt{(1-\varepsilon)m}\right]}+\frac{5}{8}\sqrt{(1-\varepsilon)m}$	A mathematical model for 2D square solid particles with m as the anisotropic parameter and θ as the tilt angle

properties of Sierpinski carpet (Feranie and Latief, 2013; Khabbazi et al., 2015). However, the unified conclusion to obtain tortuosity value remains unknown, especially for the effect of particle arrangement on tortuosity.

In this study, we obtained tortuosity by numerical simulation (CFD). The length of streamlines in the characteristic plane is calculated by accumulating the coordinate distance of each fluid particle based on Eq. (6), as shown in Fig. 2. The characteristic plane is defined as the middle height plane of the microfluidic model. That is h_1=0.025 μm, because the height of the microfluidic model used in this study was 0.05 μm. It visually indicated that streamline patterns from numerical simulation corresponded to the experimental measurements provided in Section S1 of the electronic supplementary materials (ESM).

$$l_1=\sum_i\sqrt{(x_i-x_{i-1})^2+(y_i-y_{i-1})^2}, \tag{7}$$

$$\tau=\sum_{n=1}^{I}\frac{l_n}{nL}, \tag{8}$$

where l_n is the length of the nth streamline, I is the total number of streamlines, and x_i and y_i are the coordinates of fluid particles.

3 Materials and experimental methods

3.1 Materials

Deionized (DI) water was used as the liquid phase. Monodisperse fluorescent microspheres (polystyrene microspheres) with a density and diameter of 1.05 g/cm^3 and 1.0 μm, respectively, were purchased to serve as the tracer particles. They were used to visualize the fluid streamline, which had reliable flow behavior when the diameter of fluorescent microspheres was less than 1.0 μm under laminar flow (Shen and Chen, 1989).

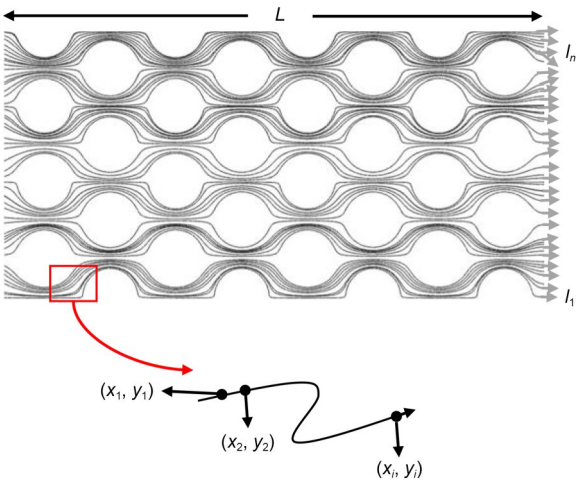

Fig. 2 Schematic diagram of streamline for microfluidic models

3.2 Experimental apparatus

The experimental system of fluorescent microscopy combined with a microfluidic chip is presented in Fig. 3. Water was injected with a syringe pump (Harvard PHD ULTAR, USA). The controllable injection rate ranged from 0.1 μL/min to 5 L/min and the injection pressure of DI water was measured with pressure sensors (uProcess Analog Sensor Manifold 4AM01, USA). We used the fluorescence microscopy method to collect images for fluid-streamline and velocity detection. All images were captured with a reverse microscope (Nikon Inverted Research Microscope ECLISE Ti2-U, Japan). Data were acquired through the CellSens software provided by Nikon.

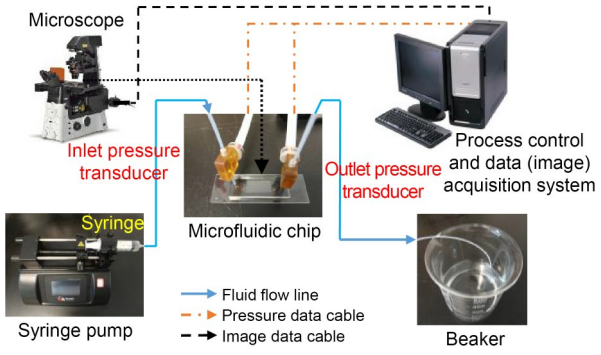

Fig. 3 Schematic of the experimental system used for pressure drop measurement

The hydrophilic borosilicate glass microchannels, consisting of micropillars, were fabricated using the deep reactive ion etching (DRIE) microfabrication technique. A schematic of the entire microfluidic chip is shown in Fig. 4a. Microchannels with dimensions of 1 cm (width)×2 cm (length)×50 μm (depth) were built into the microfluidic chip, which consisted of uniform micropillars. Branch inlet and outlet regions with a dimension of 800 μm (width)×50 μm (depth) were connected to the microchannels. The length of branch inlet or outlet regions is illustrated in Fig. 4b. For circular micropillars (Fig. 4c), we investigated square and triangular arrangements of microchannels with micropillar diameters of 500, 1000, and 2000 μm, and porosities of 0.54 and 0.60 (Table 2). The height for the square arrangement of microchannels with a micropillar diameter of 500 μm and porosity of 0.60 ranged from 30 to 200 μm. The porosity for the

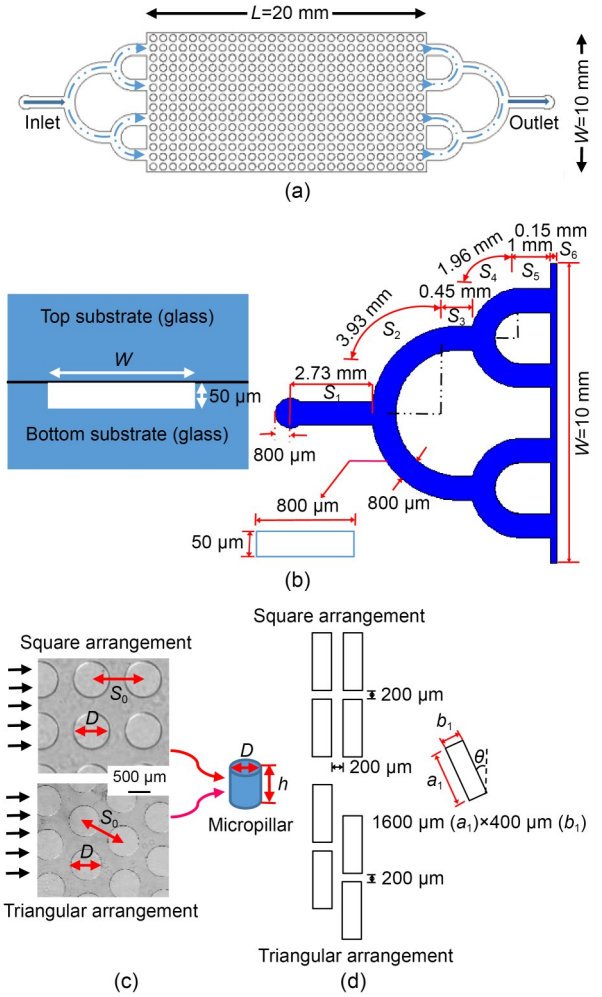

Fig. 4 (a) Schematic diagram of the microfluidic chip; (b) close-up view of the inlet port channels; (c) dimensions of circular micropillars; (d) dimensions of rectangular micropillars

Table 2 Geometrical dimensions of different microfluidic models considered in the present work

Type of microfluidic model	Micropillar shape	Micropillar arrangement	Micropillar dimension				Porosity, ε	Tilt angle, θ (°)
			D (μm)	S_0 (μm)	a_1 (μm)	b_1 (μm)		
Asq-0.60-500	Circular	Square	500	707	–	–	0.60	–
Asq-0.60-1000	Circular	Square	1000	1414	–	–	0.60	–
Asq-0.60-2000	Circular	Square	2000	2828	–	–	0.60	–
Ast-0.60-500	Circular	Triangular	500	758	–	–	0.60	–
Ast-0.60-1000	Circular	Triangular	1000	1519	–	–	0.60	–
Ast-0.60-2000	Circular	Triangular	2000	2631	–	–	0.60	–
Ast-0.54-500	Circular	Triangular	500	707	–	–	0.54	–
Ast-0.54-1000	Circular	Triangular	1000	1414	–	–	0.54	–
Ast-0.54-2000	Circular	Triangular	2000	2828	–	–	0.54	–
Asq-0.41-0°	Rectangular	Square	–	–	1600	400	0.41	0
Asq-0.41-30°	Rectangular	Square	–	–	1600	400	0.41	30
Asq-0.41-45°	Rectangular	Square	–	–	1600	400	0.41	45
Asq-0.41-60°	Rectangular	Square	–	–	1600	400	0.41	60
Asq-0.41-90°	Rectangular	Square	–	–	1600	400	0.41	90
Ast-0.41-0°	Rectangular	Triangular	–	–	1600	400	0.41	0
Ast-0.41-30°	Rectangular	Triangular	–	–	1600	400	0.41	30
Ast-0.41-45°	Rectangular	Triangular	–	–	1600	400	0.41	45
Ast-0.41-60°	Rectangular	Triangular	–	–	1600	400	0.41	60
Ast-0.41-90°	Rectangular	Triangular	–	–	1600	400	0.41	90

D is the micropillar diameter, S_0 is the distance between two neighboring micropillars, a_1 is the length of a rectangular micropillar, b_1 is the width of a rectangular micropillar, Asq indicates square arrangement, and Ast indicates triangular arrangement. For example, Asq-0.60-500 refers to a circular micropillar with square arrangement, in which the micropillar diameter is 500 μm, and the porosity is 0.60. Asq-0.41-0° refers to a rectangular micropillar with square arrangement in which the porosity is 0.41 and the tilt angle is 0°

square microchannel arrangement with a diameter of 500 μm and microchannel height of 50 μm ranged from 0.33 to 0.90.

Soils are composed of mineral grains. Grain size distribution and particle shape both play a critical role in soil macroscale behavior. Inherent fabric in non-spherical coarse-grained soils always posited a rectangular flaky particle for the conceptual model, especially for undrained strength anisotropy (Santamarina and Cho, 2004). Here, we propose a facile microfluidic model to explore the effect of anisotropy on permeability (Fig. 4d). The rectangular-micropillar model can also be used to simulate 2D fractured rock mass flow. For rectangular micropillars (Fig. 4d), the intrinsic porosity was 0.41. The unit cell size was 400 μm (b_1)× 1600 μm (a_1) and the size of the pore throat was 200 μm. The tilt angles for both triangular and square arrangements were between 0° and 90°.

3.3 Calibration of pressure drop in the microfluidic model

DI water was injected into the microchannels with the syringe pump at appropriate flow rates. No leakage was observed, and the flow was stable. We obtained the total pressure drop by subtracting outlet pressure from inlet pressure. The composition of the measured pressure drop was given by Akbari et al. (2009):

$$\Delta P_{\mathrm{F}}=\Delta P_{\mathrm{M}}-\left(\Delta P_{\mathrm{t}}+\Delta P_{\mathrm{c}}+\Delta P_{\mathrm{N}}+\Delta P_{\mathrm{D}}+\Delta P_{\mathrm{x}}+2\Delta P_{\mathrm{b}}+\Delta P_{\mathrm{v}}\right), \tag{9}$$

where ΔP_{F} is the pressure drop in the fully developed region, ΔP_{t} is the pressure loss due to flow in the tubes connecting the transducer to the microchannel inlet, ΔP_{c} is the pressure loss due to flow in the inlet and outlet channels, ΔP_{N} and ΔP_{x} are the inlet and exit

losses, ΔP_b is the pressure drop due to 90° bends, ΔP_D is the developing region loss, and ΔP_v is the pressure drop corresponding to the electro-viscous effect.

Bahrami et al. (2007) proposed a solution to determine the pressure drops in the inlet and outlet rectangular channels of a microfluidic chip. The laminar flow in microchannels is single-phase and fully developed. We observed that the Poiseuille number was only a function of geometrical parameters of the cross-section when the fluid properties and flow rates were constant. The proposed model is expressed as follows:

$$4f_f = \frac{2\Delta P D_h}{\rho u^2 L}, \tag{10}$$

$$f_f Re_{\sqrt{A}} = \frac{12}{\left[1-\frac{192}{\pi^5}\epsilon\tanh\frac{\pi}{2\epsilon}\right](1+\epsilon)\sqrt{\epsilon}}, \tag{11}$$

$$Re_{\sqrt{A}} = \frac{\rho u\sqrt{A}}{\mu}, \tag{12}$$

where f_f is the Fanning friction factor and $4f_f=f$ (Yang XH et al., 2019), ΔP is the pressure drop in the inlet and outlet rectangular channels, and u is the fluid velocity. $Re_{\sqrt{A}}$ is the Reynolds number defined based on the square root of the area, $\sqrt{A}$. $\epsilon=\frac{c}{b}$ is the aspect ratio, and b and c are the major and minor semi-axes of the cross-section with $b\geq c$. $\sqrt{A}$, as the characteristic length scale for non-circular channels, is a more appropriate length scale since it is found through analysis (Yovanovich, 1974).

ΔP_t and ΔP_v were neglected. ΔP_c was calculated based on the diameter and length of connecting tubes. ΔP_D and ΔP_v were lower than 0.3% compared to the measured pressure drop. ΔP_N, ΔP_x, and ΔP_b were lower than 1% compared to the measured pressure drop with a small Reynolds number, and lower than 5% with a larger Reynolds number (Akbari et al., 2009).

3.4 Numerical simulations

3.4.1 Physical model

Based on the experimental microfluidic chips, the dimensions of the numerical physical model are shown in Fig. 5. Upper and lower boundaries were fixed and the flow direction was from left to right. DI water was used as the fluid phase and its density and viscosity were 998.2 kg/m^3 and 0.001 kg/(m·s), respectively.

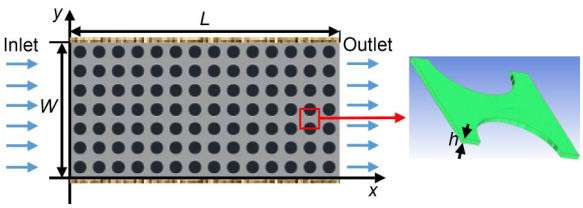

Fig. 5 Diagram of numerical physical model with model's length *L*=20 mm, inner width *W*=10 mm, and channel depth *h*=50 μm. The black circles are micropillars and the grey region is the pore channels

3.4.2 Governing equations

When the Reynolds number is small, the following assumptions are made to simplify the calculation of the numerical solution. (1) The liquid–solid interface is set to the no-slip boundary. (2) There is steady laminar flow in the microchannels. (3) The mass force item can be disregarded. (4) The physical parameters of the fluid are constant.

Then, the continuity equation for incompressible Newtonian fluid is set to be the governing equation:

$$\frac{\partial u_x}{\partial x}+\frac{\partial u_y}{\partial y}+\frac{\partial u_z}{\partial z}=0, \tag{13}$$

where u_x, u_y, and u_z are components of the water velocity. The momentum equations are:

$$u_x\frac{\partial u_x}{\partial x}+u_y\frac{\partial u_x}{\partial y}+u_z\frac{\partial u_x}{\partial z}= -\frac{1}{\rho}\frac{\partial p}{\partial x}+\mu\left(\frac{\partial^2 u_x}{\partial x^2}+\frac{\partial^2 u_x}{\partial y^2}+\frac{\partial^2 u_x}{\partial z^2}\right), \tag{14}$$

$$u_x\frac{\partial u_y}{\partial x}+u_y\frac{\partial u_y}{\partial y}+u_z\frac{\partial u_y}{\partial z}= -\frac{1}{\rho}\frac{\partial p}{\partial y}+\mu\left(\frac{\partial^2 u_y}{\partial x^2}+\frac{\partial^2 u_y}{\partial y^2}+\frac{\partial^2 u_y}{\partial z^2}\right), \tag{15}$$

$$u_x\frac{\partial u_z}{\partial x}+u_y\frac{\partial u_z}{\partial y}+u_z\frac{\partial u_z}{\partial z}= -\frac{1}{\rho}\frac{\partial p}{\partial z}+\mu\left(\frac{\partial^2 u_z}{\partial x^2}+\frac{\partial^2 u_z}{\partial y^2}+\frac{\partial^2 u_z}{\partial z^2}\right), \tag{16}$$

where p is the pressure, and μ is the kinematic viscosity of water.

3.4.3 Boundary conditions

The inlet boundary condition is given by:

$$x=0,\ u_x=u_0,\ u_y=0,\ u_z=0. \tag{17}$$

The outlet boundary condition can be written as:

$$x=L,\quad \frac{\partial u_x}{\partial x}=\frac{\partial u_y}{\partial x}=\frac{\partial u_z}{\partial x}=0. \tag{18}$$

The liquid–solid interfaces are assumed to be no-slip boundaries. Therefore, velocity at these interfaces satisfies the following relationship:

$$u_x=u_y=u_z=0. \tag{19}$$

3.4.4 Numerical approach

We used ANSYS FLUENT 2019 R3 (Canonsburg, Pennsylvania, USA), a CFD program, to simulate the seepage in 3D. A structured grid system was used to divide the computational domain in our model. The liquid phases in the microchannel were divided into hexahedral elements and local mesh refinement was conducted for the microchannel region to improve calculation accuracy. Symmetry boundary conditions were applied at the sides of the unit cell under consideration. In order to ensure the reliability of numerical results, we conducted a grid independence test (Fig. 6a). At a velocity of 3.3×10^{-4} m/s, the inlet pressure increased with more grid-node numbers. When the number of grid nodes (N) was over 1.1×10^{6}, inlet pressure reached equilibrium. The maximum grid size was 0.02 mm.

We used the SIMPLEC algorithm to calculate the pressure–velocity coupling. For better convergence accuracy of the calculation, we applied the Gauss-Seidel method, taking into consideration the over-relaxation factor. We adopted the double precision, and discretized the momentum equation using a second-order upwind scheme. The relaxation factor was set to 0.5, and the residual between the two iteration steps was set to 1×10^{-6}. When the maximum residuals of velocity were 1×10^{-6}, the iteration was regarded as convergent. A comparison between the numerical and experimental results for the inlet pressure of Asq-0.60-1000 is given in Fig. 6b. The maximum deviation between the numerical and experimental results was 14.7%. It was under control, and thus we considered the current model to be reasonable and able to predict the seepage characteristics of the microfluidic chip model.

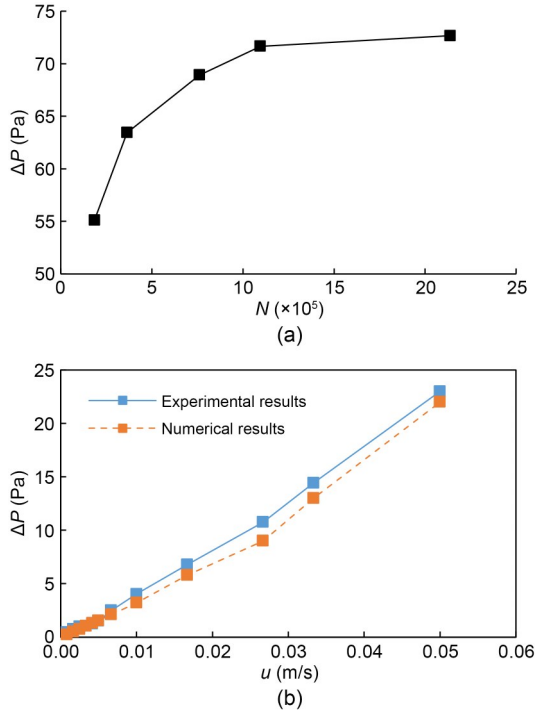

Fig. 6 (a) Grid independence test; (b) validation of numerical microfluidic chip model of Asq-0.60-1000

4 Results and discussion

4.1 Effects of porosity on tortuosity

Fig. 7 presents a tortuosity comparison between numerical simulations of square and triangular arrangements and models in previous studies (with porosity ranging from 0.3 to 1.0). Generally, tortuosity appears to decrease as the porosity increases. The traditional assumption is that tortuosity is only dependent on

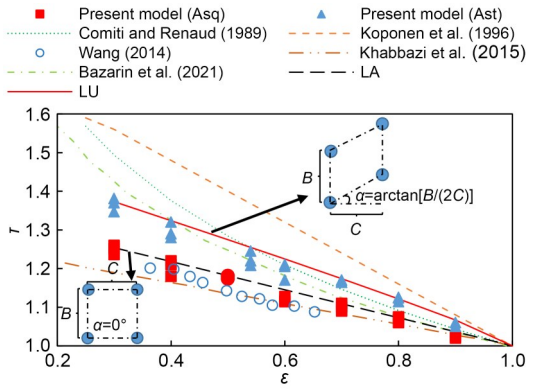

Fig. 7 Comparison of tortuosity between numerical simulations and models in the literature. *B* is the vertical distance between adjacent micro columns, *C* is the horizontal distance between adjacent micro columns, and other parameters are explained in the text. LA represents the line of lower-limit arrangement, and LU represents the line of upper-limit arrangement

porosity (Koponen et al., 1996; Wang, 2014; Khabbazi et al., 2015), but the 2D particle arrangement also has an effect on it. In our experiments, we found that with the same porosity, models with triangular arrangement always yielded higher tortuosity than those with square arrangement. For example, the tortuosity of Ast-0.60-500 was 1.21, higher than that of Asq-0.60-500 (1.13), which means that the flow path would be more tortuous with a triangular arrangement than with a square arrangement. This is evident in Fig. 7. On the other hand, as the porosity increased from 0.30 to 1.00, the tortuosity for the triangular arrangement decreased from 1.37 to 1.00, while it decreased from 1.26 to 1.00 for the square arrangement. The deviation between triangular and square arrangements with the same porosity decreased as porosity increased. This result indicated that the particle obstruction to the fluid weakened when the porosity increased from 0.30 to 1.00.

The relationship between tortuosity and porosity has been reported extensively, as shown in Table 1. Results obtained by Koponen et al. (1996) and Khabbazi et al. (2015) showed that tortuosity decreases linearly when porosity increases. Yet, Comiti and Renaud (1989) and Bazarin et al. (2021) proposed a nonlinear relationship. In this study, models were postulated for 2D uniform porous media and no-slip boundary conditions. Khabbazi et al. (2015) obtained an analytical tortuosity–porosity correlation for a 2D circular-based Sierpinski carpet with a square arrangement, which was consistent with our experimental results for the model with the square arrangement. Meanwhile, the tortuosity of our experimental model with the triangular arrangement was roughly similar to that of the model proposed by Bazarin et al. (2021), in which the fractal geometry of a 2D Sierpinski carpet was solved by the LBM. However, it is notable that when the porosity was larger than 0.7, the numerical tortuosity of our triangular-arrangement models was higher than that obtained by Bazarin et al. (2021). The deviation may be due to the assumption in their study of fractal geometry of square particles, while uniform circular particles were used in this study. Furthermore, because of the different assumptions and boundary effects, such as particle size and shape (Comiti and Renaud, 1989; Koponen et al., 1996; Wang, 2014), 2D vs. 3D random particle-arrangement simulation (Bazarin et al., 2021), and topological properties of Sierpinski carpet (Khabbazi et al., 2015), value deviations of tortuosity existed in all these tortuosity models, as shown in Fig. 7. However, they all presented the negative tendency between the tortuosity and porosity.

We proposed a mathematical model for calculating 2D circular-based soil tortuosity for different particle arrangements:

$$\tau=\frac{1}{\cos\left[(1-\varepsilon)^{\frac{1}{3}}\alpha\right]}+\left(\frac{\pi}{4}-\frac{1}{2}\right)\frac{4(1-\varepsilon)}{\pi}, \quad (20)$$

where α is the horizontal angle between two particles, which arranges from 0° to arctan[B/(2C)]. As shown in Fig. 7, the special case when α=0° is defined as the line of lower-limit arrangement (LA), and the normal case when α=arctan[B/(2C)] is defined as the line of upper-limit arrangement (LU). More details are shown in Section S2 of the ESM.

4.2 Effects of Reynolds number on permeability

The relationship between the permeability and Reynolds number of sample Asq-0.60 is depicted in Fig. 8. Generally, microfluidic chips with larger micropillar diameters induced larger permeability compared to those with smaller micropillar diameters in both experiments and numerical simulations. The ratios of micropillar wetted surface area to channel side wall area ($L\times W$) for Asq-0.60-500, Asq-0.60-1000, and Asq-0.60-2000 were 15.39, 7.70, and 4.40, respectively. With greater micropillar diameter, the unit micropillar wetted surface area decreased, causing the side friction to decrease in turn. Therefore, microfluidic

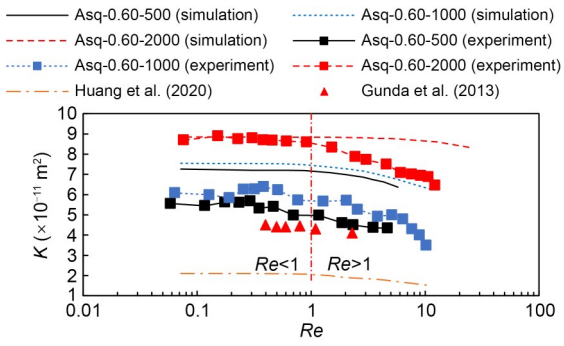

Fig. 8 Effects of Reynolds number on permeability of square-arrangement microfluidic chips with a porosity of 0.60

chips with smaller micropillar diameters yielded lower permeability than those with larger micropillar diameters, with the same porosity.

As shown in Fig. 8, when the Reynolds number Re<1, the permeability was almost independent of the Reynolds number, which was quite obvious in the numerical simulation results. Further increase in the Reynolds number led to lower permeability. Huang et al. (2020) developed a heterogeneous numerical model of laminar flow in 2D porous media. The correlation they found between permeability and Reynolds number was in line with the results mentioned above. The same conclusion was also obtained in microfluidics experiments done by Gunda et al. (2013). This was because the Darcy law could not accurately describe the seepage characteristics of the porous media when Re>1. When the Reynolds number is large, it was proved that the liquid flow in porous media is affected by both inertial and viscous forces, and the side friction increases (Antohe et al., 1997). Based on the Darcy-Forchheimer law, Eq. (2) can be rewritten to the following expression:

$$-\frac{\mathrm{d}p}{U\mathrm{d}x}=\frac{\mu}{K}+\delta\rho U. \tag{21}$$

We obtained the relationship diagram for $\frac{\Delta p}{UL}$ and U, which enabled us to calculate the permeability by the intercept. The inertial resistance coefficient δ (m^{-1}) was calculated by the slope, and was found to be 62456, 64689, and 82125 for Asq-0.60-500, Asq-0.60-1000, and Asq-0.60-2000, respectively.

The permeability obtained with our numerical simulations was about 10% higher than that obtained in the experiments (Fig. 8). We proposed the following explanations for this discrepancy: (1) no-slip boundary conditions and smooth sides were applied in the numerical simulation, but side friction was included in the experiments; (2) the pressure drop caused by inlet and exit losses and the electro-viscous effect were neglected; (3) the hydraulic pressure measured by pressure sensors varied in the experiments.

4.3 Effects of micropillar arrangement on permeability

Flow characteristics including pressure distribution and velocity vector distribution for models Ast-0.60-2000 and Asq-0.60-2000 at a velocity of 3.3×10^{-4} m/s, are demonstrated in Fig. 9. With the same porosity, the triangular-arrangement model yielded a larger pressure drop (65 Pa) than the square-arrangement model (57 Pa). The maximum pressure was in the inlet, and it decreased with the flow direction. The maximum velocity in the pore throat of the triangular-arrangement model was 1.78×10^{-3} m/s, higher than that of the square-arrangement model (1.53×10^{-3} m/s). We observed that flow in the triangular-arrangement model was divided

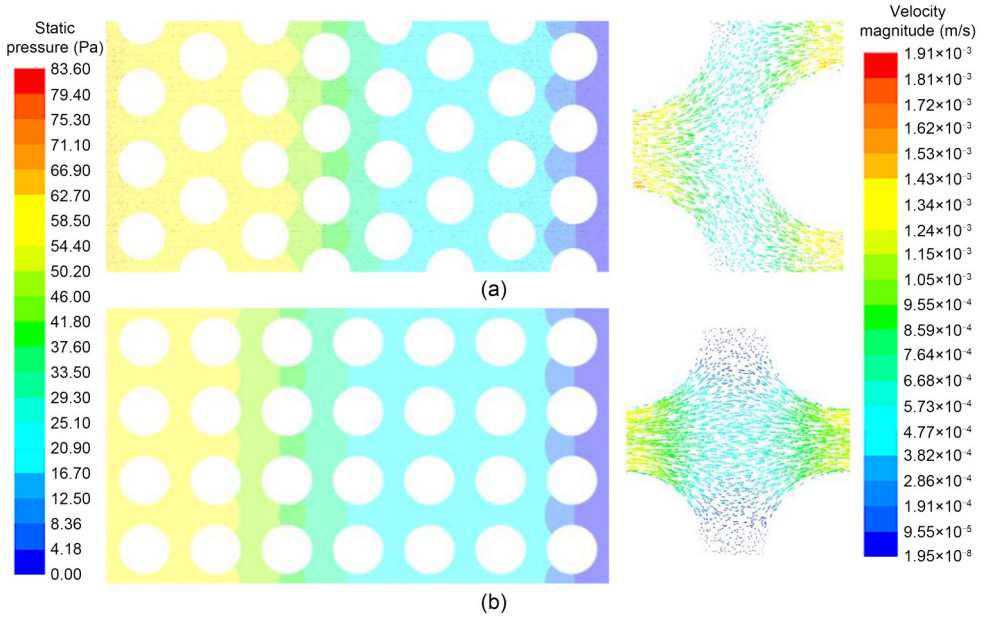

Fig. 9 Effects of micropillar arrangement on pressure distribution and velocity vector distribution at a velocity of 3.3×10^{-4} m/s: (a) Ast-0.60-2000; (b) Asq-0.60-2000. References to color refer to the online version of this figure

into two parts, causing the difficulty of flow seepage and increasing of flow path. However, the flow seeped mostly straight in the horizontal pore-channel direction in the square-arrangement model. The velocity in the vertical pore throat was nearly zero.

To further investigate the effect of micropillar arrangement on the permeability of microfluidic chips, we considered microchannels with square and triangular micropillar arrangements and a porosity of 0.60. A comparison of experimental permeabilities with different micropillar arrangements is presented in Fig. 10. With the same micropillar diameter D, the triangular-arrangement model yielded a lower permeability (4.5%–7.4%) than the square-arrangement model. This difference was more pronounced with larger micropillar diameters. When the porosity and micropillar diameter are the same, tortuosity is the only variable parameter based on the KC equation, which has an effect on the permeability of microfluidic chips. From Fig. 7, one can see that the tortuosity values in the triangular-arrangement model were 5.1%–7.9% higher than those in the square-arrangement model, with a porosity of 0.60. This deviation led to a difference in permeability of the microfluidic models with different arrangements.

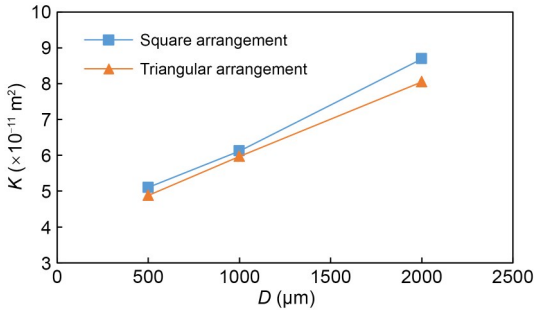

Fig. 10 Comparison of experimental permeabilities with different micropillar arrangements and a porosity of 0.60

4.4 Effects of anisotropy on permeability

The effects of tilt angle on the tortuosity and velocity vector of the unit-cell model with rectangular micropillar arrangement are shown in Fig. 11a. With the same tilt angle, the tortuosity of the triangular-arrangement model was higher than that of the square-arrangement model. In the triangular-arrangement model, we observed that the larger the tilt angle, the lower the tortuosity and velocity in the microchannel. The maximum tortuosity was 2.0397 when the tilt angle was 0°. When the tilt angle was 90°, the tortuosity was nearly 1.0, which was caused by the horizontal direction channel of preferential flow. The same tendency was also presented in the square-arrangement model, except for a tilt angle of 0°, at which the tortuosity was only 1.0389, far lower than the value (1.3918) when the tilt angle was 30°. In addition, when the tilt angle was 0°, the velocity vector of the square-arrangement model was almost in the horizontal flow direction channel and the velocity magnitude was as high as 5.95×10^{-3} m/s, which was higher than those in other models. This can be explained by the fact that the flow rate was constant and the velocity was in reverse proportion to the flow area.

Based on the microfluidic chip's geometrical structure, we obtained a geometric solution for each microfluidic model (Fig. 11a). The geometric solutions

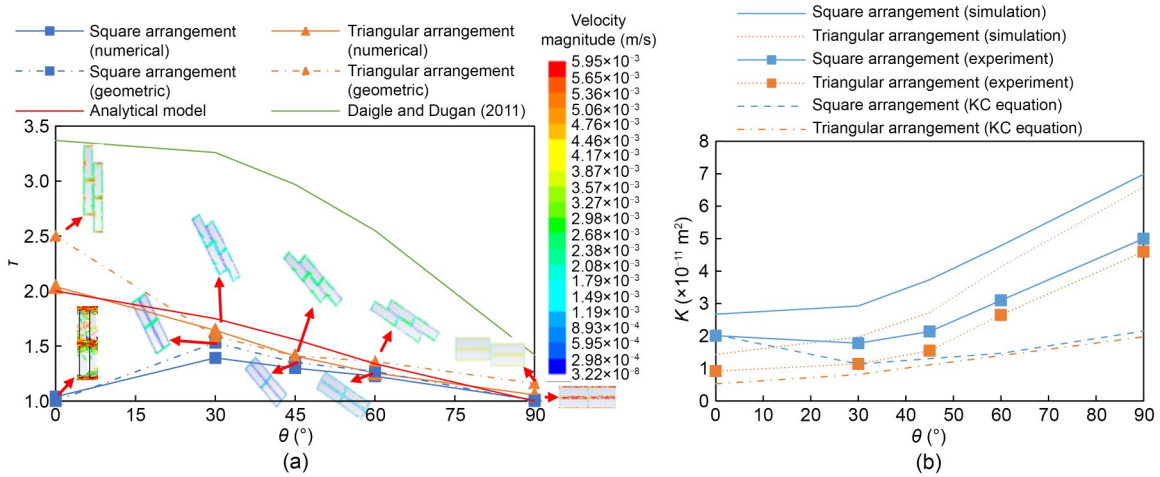

Fig. 11 Effects of tilt angle on tortuosity (a) and permeability (b). References to color refer to the online version of this figure

were generally consistent with those determined by numerical simulation. However, the general observation was that results obtained by geometric solution were higher than those obtained by numerical simulation, especially for the triangular-arrangement model with a tilt angle of 0°. The geometric solution was 2.50, 25% higher than the numerical solution. The assumption of geometric analysis was that the streamline was a straight line in the center of the microchannel, while the streamlines were curves in the numerical simulation, as shown in Fig. 11a. More details are given in Section S3 of the ESM.

Due to the high aspect ratio, fabric in clay-rich sediments was reoriented during consolidation and shearing, causing a change in permeability. Daigle and Dugan (2011) developed a model to describe the development of permeability anisotropy; it took into consideration the grain aspect ratio, porosity, and average angle of grains with respect to the horizontal plane. Results obtained by numerical simulation were compared to this model. It was clear that the model could not predict the numerical results accurately, because it produced far higher values than those acquired by numerical simulation. In the model, fabric particles were assumed to be flat cylindrical grains, while a 2D rectangular particle was idealized in this study. Thus, we proposed an analytical model based on 2D rectangular particles (Section S4 of the ESM):

$$\tau = 1 + \frac{r^2\cos^2\theta}{\left(\dfrac{3\varepsilon}{1-\varepsilon}+2\right)(r\cos\theta+\sin\theta)}, \tag{22}$$

where r is the aspect ratio. As shown in Fig. 11a, the results from the analytical model correspond to the numerical results.

Based on the results shown in Fig. 11a, we determined the effects of anisotropy on permeability by varying the tilt angle of unit cells (Fig. 11b). Several general observations were obtained. At the same tilt angle, we observed lower permeability in the triangular-arrangement model than in the square-arrangement model, in both the numerical simulation and KC equation. With the same arrangement, the permeability of microfluidic models increased by nearly four times as the tilt angle increased from 0° to 90°. Equivalent permeability of 2D fractured rock-mass flow with different direction angles was discussed by Wang (2014). The same result: the equivalent permeability increased with the tilt angles, was obtained. Compared to the experimental permeability, numerical simulation led to higher permeability for the same model, while the KC equation led to lower permeability. The deviation was in two times. This indicated that the KC equation could roughly predict the permeability of the microfluidic test under the effects of anisotropy.

For the rectangular-micropillar model, the shape factor was the same. It was noted that the tortuosity was only 1.0389, yet the permeability was 2.03×10^{-11} m^2 for the square-arrangement model with a tilt angle of 0°. The effective porosity of this model was only 0.12, far lower than its intrinsic porosity of 0.41. The effective porosity is defined as the ratio of the pore volume with streamlines to the total volume. Due to the pore structure and wall effect of the microfluidic model with the rectangular-micropillar arrangement, the phenomenon of preferential flow was clearly observed, as shown in Fig. 11a. Although the pore channels were interconnected, the streamlines only existed in the pore channel of flow direction. Thus, compared to tortuosity, porosity had a more considerable influence on the permeability of porous media.

4.5 Effects of tortuosity on permeability

The effects of tortuosity on permeability in the experimental models are depicted in Fig. 12. As expected, there was an inverse relationship between permeability and tortuosity. Permeability was found to decrease with an increase in tortuosity. The coefficient of determination R^2 for the rectangular-micropillar models and circular-micropillar models, as well as the results of Li et al. (2019), were 0.9639, 0.8962, and 0.9163, respectively. These values are all higher than 0.80, which means that the linear regression model fits the correlation between permeability and tortuosity. It is observed that the fitting coefficients for these three models were −57.237, −6.6, and −2.5226, respectively. Compared to the circular-micropillar models and the results of Li et al. (2019), the permeability of the rectangular-micropillar models was the most sensitive to change in tortuosity. This is because the porosity increased from 0.33 to 0.90 for the rectangular-micropillar models, while the porosity for the circular-micropillar models was 0.41, and it was 0.30 for the models designed by Li et al. (2019). Compared to tortuosity, permeability is more sensitive to porosity.

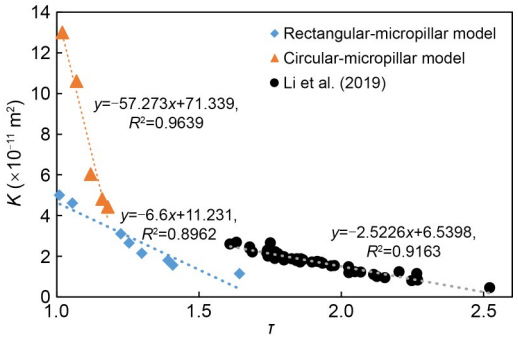

Fig. 12 Variation of permeability with tortuosity

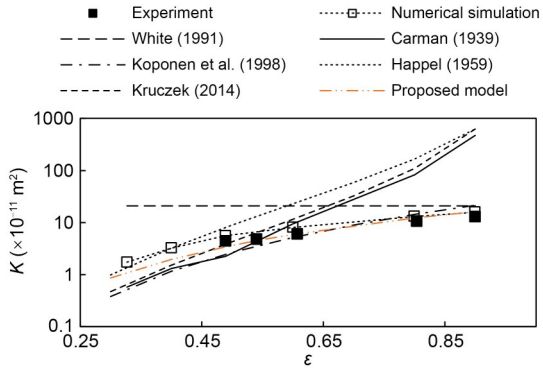

Fig. 13 Comparison of permeabilities obtained from experiment and numerical simulation with those obtained from formulas available in the literature for Asq-500

When the porosity is constant, the permeability anisotropy ratio can be defined as the ratio of horizontal permeability to vertical permeability: $\delta_0 = K_h/K_v$ (Daigle and Dugan, 2011). For the circular-micropillar models and models of Li et al. (2019), the anisotropy ratio is defined as the ratio of maximum to minimum permeability. Therefore, the anisotropy ratio for the circular-micropillar models is 5.43, while it is 3.28 for the models designed by Li et al. (2019). The latter were 3D digital cores of tight sandstone. Overall, the higher the anisotropy ratio, the larger the change in permeability.

4.6 Effects of porosity on permeability

As a structural parameter, porosity plays a key role in permeability, especially when it is small. In the current work, the pores of microfluidic chip models were interconnected. In Fig. 13, permeabilities generated by experiment and numerical simulation for Asq-500 are compared with permeabilities obtained from formulas available in the literature (Carman, 1939; Happel, 1959; White, 1991; Koponen et al., 1998; Kruczek, 2014). Details of these formulas are displayed in Table 3. Permeability generated by numerical simulation was consistent with that obtained from experiments, and the error was 9.78%–28.43%. The permeability prediction equations displayed in Table 3 are either the KC equation or modified KC equations, except the White equation (White, 1991). For parallel-plate duct flow, the equivalent permeability can be expressed by the White equation (White, 1991). However, all the KC equations and modified KC equations fail to predict the permeability of microfluidic models accurately. For example, permeability estimated by the classic KC equation with the values of tortuosity in Fig. 8 roughly agreed with experimental results when the porosity was only in the range of 0.50–0.60. When the porosity was lower than 0.50, the permeability estimated by the KC equation was lower than the experimental results, and the error was within one time. When the porosity was higher than 0.60, the permeability estimated by the KC equation was higher than

Table 3 Predicted equations of permeability in the literature

Reference	Model for permeability	Note
Carman (1939)	$K=\frac{1}{C_0\tau^2S^2}\frac{\varepsilon^3}{(1-\varepsilon)^2}$	
Happel (1959)	$K=\frac{d^2}{32(1-\varepsilon)}\left[-\ln(1-\varepsilon)+\frac{(1-\varepsilon)^2-1}{(1-\varepsilon)^2+1}\right]$	d is defined as the mean particle diameter
White (1991)	$K=\frac{h_0^2}{12}$	h_0 is the height of the duct
Koponen et al. (1998)	$K=\frac{\varepsilon^3}{C_0S_R^2}$	C_0 is 2 for cylindrical capillaries; S_R is the ratio of fluid–solid interfacial area to total sample volume
Kruczek (2014)	$K=\frac{\Phi_s^2d_p^2}{180}\frac{\varepsilon^3}{(1-\varepsilon)^2}$	Φ_s is the sphericity of the particles in the packed bed; d_p is the diameter of the equivalent spherical particle

the experimental results, and the error increased with the porosity increment. It was observed that the error was more than one order of magnitude. The KC equation is not suitable for porosities above 0.60 (Koponen et al., 1998; Miguel, 2012; Sharma et al., 2023). It was also observed that the Koponen equation (Koponen et al., 1998) had the potential to predict the experimental results fairly accurately. Yet, it only fitted the experimental points when porosity ranged from 0.60 to 0.80. When the porosity exceeded 0.80 or was below 0.60, the error was as high as 71%.

When porosity was close to 1.0, the flow characteristics in the microfluidic chip model and the parallel-plate duct flow model (White, 1991) were similar. This tendency is clear in Fig. 13. With a porosity of 1.0, the permeability obtained by White (1991) was 2.08×10^{-10} m^2, while that obtained by numerical simulation was 2.23×10^{-10} m^2. Based on the above analysis and literature research, a predicted model for the permeability of a microfluidic model was proposed:

$$K=\frac{1}{c\tau}\varepsilon^2 r_{\mathrm{cr}}^2, \tag{23}$$

where r_{cr} is the pore radius, and c is a shape parameter. For a quasi-two-dimensional microfluidic model, c is 3.4 (Mathavan and Viraraghavan, 1992). Carman (1956) proposed the hydraulic radius as a candidate for the pore radius, which is defined by the ratio of total pore volume to the total wetted surface area. The plot depicted in Fig. 13 shows that the porosity is 0.60, and the permeability values obtained by the proposed model and experiment are 6.07×10^{-11} and 6.02×10^{-11} m^2, respectively. The permeability obtained by the proposed model can be in line with the experimental results. In addition, the permeability obtained by the proposed model is about 40% below the numerical results when the porosity is lower than 0.60. On the other hand, it matches the numerical results for high porosities, especially for a porosity of 0.90. In short, the permeability of microfluidic models generated by the proposed model can predict the experimental and numerical results well compared to other equations in the literature.

To validate the applicability of the predicted model, a comparison of experimental results obtained by Gunda et al. (2013) with the results of the predicted model is displayed in Fig. 14. In the experiments of Gunda et al. (2013), the micropillars were arranged in a square formation and the porosity of the microfluidic models ranged from 0.50 to 0.95. The predicted model appears to succeed in presenting the varying permeability of structured porous media.

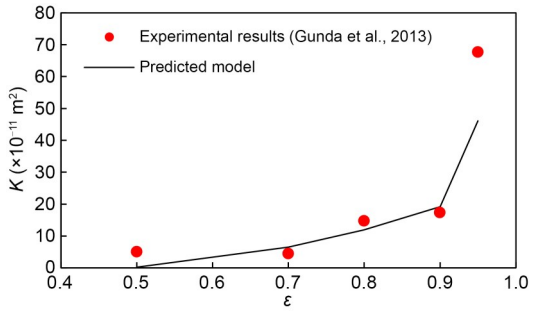

Fig. 14 Comparison of experimental results (Gunda et al., 2013) with those of the predicted model

4.7 Sources of error

Comparison of the experimentally derived permeability values with the numerical simulation and different models for Asq-0.60-500, was plotted as a function of microchannel depth (Fig. 15). Compared to experimental results, numerical simulation induced 25%–43% higher permeability values with the same microchannel depth, and the deviation increased proportionally to the channel depth increase. It was evident that microchannel depth was one important source of error. When the microchannel depth was 30 μm, both models could accurately predict the permeability of the microfluidic chips; but when the microchannel depth was larger than 50 μm, the KC equation failed to predict the permeability accurately. At the same time,

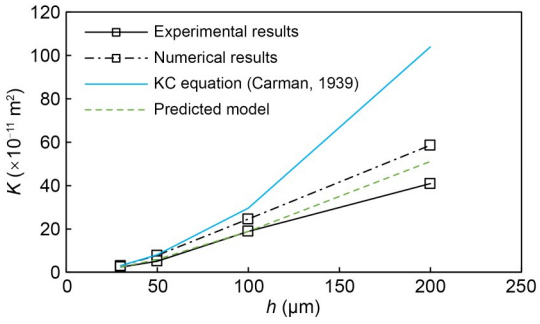

Fig. 15 Comparison of experimental permeability with numerical simulation and different models of Asq-0.60-500 plotted as a function of microchannel depth (h)

when microchannel depth increased from 30 to 100 μm, the permeability generated by the predicted model was very consistent with the experimental data. When the microchannel depth was 200 μm, the permeability obtained by the predicted model was 5.12×10^{-10} m^2, while that obtained in the experiment was 4.09×10^{-10} m^2.

There was a limitation to the above permeability prediction models. In the KC equation, the KC constant was affected by porosity, porous microstructure, tortuosity, and other factors. It was to be 5.0 for porous media with spherical particles based on generous experiments (Kaviany, 1995). For the peat bed, however, the KC constant was 3.4 (Mathavan and Viraraghavan, 1992). For Asq-0.60-500, the tortuosity was about 1.2, so the KC constant was 3.6. However, the KC constant did not remain constant when the microchannel depth increased from 30 to 200 μm. Meanwhile, the specific surface area decreased from 0.111 to 0.019 m^{-2} when the microchannel depth increased from 30 to 200 μm. The predicted model was meant to represent a quasi-two-dimensional porous medium with numerical simulation, and was applicable to microfluidic chip models. However, when the microchannel depth was 200 μm, the flow in microchannel pores was closer to 3D conditions. Thus, there was an error in the results. In addition, micropillars in the microfluidic models were fabricated in a uniform periodic arrangement. Yet, the type of packing and geometry of solid parts play the main relevant role in permeability (Koponen et al., 1997, 2017; Serrenho and Miguel, 2011), and therefore warrant further study.

5 Conclusions

We estimated permeability for single-phase flow through microfluidic models with integrated micropillars, with Reynolds numbers varying between 0.83 and 142.98. The experimental results were compared with those obtained by numerical simulation and empirical theoretical models. The following conclusions can be drawn:

(1) Anisotropy induced by the tilt angle (0°–90°) of rectangular micropillars formed preferential flow and decreased the effective porosity. Especially for the square-arrangement model with a tilt angle of 0°, the tortuosity was only 1.0389, yet the permeability was 2.03×10^{-11} m^2. The effective porosity of this model was only 0.12, far lower than its intrinsic porosity of 0.41. The permeability of the various models increased by nearly four times as the tilt angle increased from 0° to 90°. When the tilt angle increases from 0° to 90°, the tortuosity declines from 2.04 to 1.03, causing the permeability to rise from 1.0×10^{-11} to 4.3×10^{-11} m^2. Therefore, an analytical tortuosity model based on the 2D rectangular particles is proposed.

(2) We observed that the threshold of the Reynolds number was 1. When *Re* is below the threshold, the permeability is independent of the Reynolds number. When *Re* is over this threshold, the viscous force plays a dominant role and the permeability drops as the Reynolds number increases.

(3) The permeability of the microfluidic chip models is influenced by the diameter, arrangement, and shape of the micropillars. With the same porosity, due to the increase in side friction, microfluidic chips with smaller micropillar diameters yielded lower permeability than those with larger micropillar diameters; the permeability of triangular-arrangement model is 4.5%–7.4% lower than that of the square-arrangement model, due to a 5.1%–7.9% increase in tortuosity. Based on this, a mathematical model for calculating 2D circular-based soil tortuosity with different particle arrangements is proposed.

(4) The permeability generated by numerical simulation is consistent with that obtained from experiments, and the error is 9.78%–28.43%. However, permeability estimated by the classic KC equation roughly agrees with experimental results when the porosity is only 0.50–0.60. It was proved that the predicted model is suitable for estimating the experimental permeability of microfluidic models.

(5) As microchannel depth increases from 30 to 200 μm, the permeability obtained by numerical simulations is 25%–43% higher than that obtained by experiments. When the microchannel depth is more than 50 μm, the KC equation fails to predict the permeability of microfluidic chip models. The predicted model is therefore suitable for estimating experimental permeability with microchannel depths ranging from 30 to 200 μm.

Acknowledgments

This work is supported by the Basic Science Center Program for Multiphase Evolution in Hypergravity of the National Natural Science Foundation of China (No. 51988101), the National Natural Science Foundation of China (No. 42177118),

and the Program of Introducing Talents of Discipline to Universities (111 Project) of China (No. B18047).

Author contributions

Shaokai NIE established the experiments, implemented the numerical simulation, and wrote the first draft of the manuscript. Pengfei LIU, Kexin CHEN, and Wenyuan WANG helped to analyze the results. Yunmin CHEN provided important suggestions on the improvement of the study. Bate BATE revised and edited the final version.

Conflict of interest

Shaokai NIE, Pengfei LIU, Kexin CHEN, Wenyuan WANG, Yunmin CHEN, and Bate BATE declare that they have no conflict of interest.

References

Akbari M, Sinton D, Bahrami M, 2009. Pressure drop in rectangular microchannels as compared with theory based on arbitrary cross section. *Journal of Fluids Engineering*, 131(4):041202. https://doi.org/10.1115/1.3077143

Antohe BV, Lage JL, Price DC, et al., 1997. Experimental determination of permeability and inertia coefficients of mechanically compressed aluminum porous matrices. *Journal of Fluids Engineering*, 119(2):404-412. https://doi.org/10.1115/1.2819148

Auset M, Keller AA, 2004. Pore-scale processes that control dispersion of colloids in saturated porous media. *Water Resources Research*, 40(3):W03503. https://doi.org/10.1029/2003WR002800

Bahrami M, Yovanovich MM, Culham JR, 2007. A novel solution for pressure drop in singly connected microchannels of arbitrary cross-section. *International Journal of Heat and Mass Transfer*, 50(13-14):2492-2502. https://doi.org/10.1016/j.ijheatmasstransfer.2006.12.019

Bate B, Chen C, Liu PF, et al., 2022. The migration and deposition behaviors of montmorillonite and kaolinite particles in a two-dimensional micromodel. *Materials*, 15(3):855. https://doi.org/10.3390/ma15030855

Bazarin RLM, de Lai FC, Naaktgeboren C, et al., 2021. Boundary effects on the tortuosity and permeability of idealized porous media. *Transport in Porous Media*, 136(3):743-764. https://doi.org/10.1007/s11242-020-01530-w

Bazylak A, Berejnov V, Markicevic B, et al., 2008. Numerical and microfluidic pore networks: towards designs for directed water transport in GDLs. *Electrochimica Acta*, 53(26):7630-7637. https://doi.org/10.1016/j.electacta.2008.03.078

Cai JC, Hu XY, Standnes DC, et al., 2012. An analytical model for spontaneous imbibition in fractal porous media including gravity. *Colloids and Surfaces A: Physicochemical and Engineering Aspects*, 414:228-233. https://doi.org/10.1016/j.colsurfa.2012.08.047

Cao SC, Jung J, Radonjic M, 2019. Application of microfluidic pore models for flow, transport, and reaction in geological porous media: from a single test bed to multifunction real-time analysis tool. *Microsystem Technologies*, 25(11):4035-4052. https://doi.org/10.1007/s00542-019-04612-y

Cardona A, Santamarina JC, 2020. Carbonate rocks: matrix permeability estimation. *AAPG Bulletin*, 103(1):131-144. https://doi.org/10.1306/05021917345

Carman PC, 1939. Permeability of saturated sands, soils and clays. *The Journal of Agricultural Science*, 29(2):262-273. https://doi.org/10.1017/S0021859600051789

Carman PC, 1956. Flow of Gases Through Porous Media. Academic Press, New York, USA.

Castillo-Araiza CO, Lopez-Isunza F, 2008. Hydrodynamic models for packed beds with low tube-to-particle diameter ratio. *International Journal of Chemical Reactor Engineering*, 6(1):A1. https://doi.org/10.2202/1542-6580.1550

Chen C, 2021. Study on Fine Particle Migration and Permeability Characteristics in Porous Media Based on Microfluidic Chips. MS Thesis, Zhejiang University, Hangzhou, China (in Chinese).

Chen C, Nie SK, Liu PF, et al., 2021. Permeability characteristics of porous media based on 2D microfluidic chips. *Journal of Central South University (Science and Technology)*, 52(9):3295-3302 (in Chinese). https://doi.org/10.11817/j.issn.1672-7207.2021.09.031

Chen KX, Liu PF, Wang WY, et al., 2023. Effects of capillary and viscous forces on two-phase fluid displacement in the microfluidic model. *Energy & Fuels*, 37(22):17263-17276. https://doi.org/10.1021/acs.energyfuels.3c03170

Collins RE, 1961. Flow of Fluids Through Porous Materials. Reinhold Publishing Corporation, New York, USA.

Comiti J, Renaud M, 1989. A new model for determining mean structure parameters of fixed beds from pressure drop measurements: application to beds packed with parallelepipedal particles. *Chemical Engineering Science*, 44(7):1539-1545. https://doi.org/10.1016/0009-2509(89)80031-4

Conn CA, Ma K, Hirasaki GJ, et al., 2014. Visualizing oil displacement with foam in a microfluidic device with permeability contrast. *Lab on a Chip*, 14(20):3968-3977. https://doi.org/10.1039/C4LC00620H

Daigle H, Dugan B, 2011. Permeability anisotropy and fabric development: a mechanistic explanation. *Water Resources Research*, 47(12):W12517. https://doi.org/10.1029/2011WR011110

De S, Krishnan P, van der Schaaf J, et al., 2018. Viscoelastic effects on residual oil distribution in flows through pillared microchannels. *Journal of Colloid and Interface Science*, 510:262-271. https://doi.org/10.1016/j.jcis.2017.09.069

Dybbs A, Edwards RV, 1984. A new look at porous media fluid mechanics—Darcy to turbulent. *In*: Bear J, Corapcioglu MY (Eds.), Fundamentals of Transport Phenomena in Porous Media. Springer, Dordrecht, the Netherlands, p.199-256. https://doi.org/10.1007/978-94-009-6175-3_4

Feranie S, Latief FDE, 2013. Tortuosity-porosity relationship in two-dimensional fractal model of porous media. *Fractals*, 21(2):1350013. https://doi.org/10.1142/S0218348X13500138

Gunda NSK, Joseph J, Tamayol A, et al., 2013. Measurement of pressure drop and flow resistance in microchannels with integrated micropillars. *Microfluidics and Nanofluidics*, 14(3):711-721. https://doi.org/10.1007/s10404-012-1089-1

Happel J, 1959. Viscous flow relative to arrays of cylinders. *AIChE Journal*, 5(2):174-177. https://doi.org/10.1002/aic.690050211

Hu R, Wan JM, Yang ZB, et al., 2018. Wettability and flow rate impacts on immiscible displacement: a theoretical model. *Geophysical Research Letters*, 45(7):3077-3086. https://doi.org/10.1002/2017GL076600

Huang YP, Yao F, Zhou B, et al., 2020. Numerical study on permeability characteristics of fractal porous media. *Chinese Physics B*, 29(5):054701. https://doi.org/10.1088/1674-1056/ab7b53

Kaviany M, 1995. Principles of Heat Transfer in Porous Media. Springer, New York, USA. https://doi.org/10.1007/978-1-4612-4254-3

Kawagoe Y, Oshima T, Tomarikawa K, et al., 2016. A study on pressure-driven gas transport in porous media: from nanoscale to microscale. *Microfluidics and Nanofluidics*, 20(12):162. https://doi.org/10.1007/s10404-016-1829-8

Khabbazi AE, Hinebaugh J, Bazylak A, 2015. Analytical tortuosity–porosity correlations for Sierpinski carpet fractal geometries. *Chaos, Solitons & Fractals*, 78:124-133. https://doi.org/10.1016/j.chaos.2015.07.019

Koponen A, Kataja M, Timonen J, 1996. Tortuous flow in porous media. *Physical Review E*, 54(1):406-410. https://doi.org/10.1103/PhysRevE.54.406

Koponen A, Kataja M, Timonen J, 1997. Permeability and effective porosity of porous media. *Physical Review E*, 56(3):3319-3325. https://doi.org/10.1103/PhysRevE.56.3319

Koponen A, Kandhai D, Hellén E, et al., 1998. Permeability of three-dimensional random fiber webs. *Physical Review Letters*, 80(4):716-719. https://doi.org/10.1103/PhysRevLett.80.716

Koponen A, Ekman A, Mattila K, et al., 2017. The effect of void structure on the permeability of fibrous networks. *Transport in Porous Media*, 117(2):247-259. https://doi.org/10.1007/s11242-017-0831-2

Koşar A, Mishra C, Peles Y, 2005. Laminar flow across a bank of low aspect ratio micro pin fins. *Journal of Fluids Engineering*, 127(3):419-430. https://doi.org/10.1115/1.1900139

Kruczek B, 2014. Carman–Kozeny equation. *In*: Drioli E, Giorno L (Eds.), Encyclopedia of Membranes. Springer, Berlin, Germany, p.1-3. https://doi.org/10.1007/978-3-642-40872-4_1995-1

Kumar A, Reddy RG, 2003. Modeling of polymer electrolyte membrane fuel cell with metal foam in the flow-field of the bipolar/end plates. *Journal of Power Sources*, 114(1):54-62. https://doi.org/10.1016/S0378-7753(02)00540-2

Lanfrey PY, Kuzeljevic ZV, Dudukovic MP, 2010. Tortuosity model for fixed beds randomly packed with identical particles. *Chemical Engineering Science*, 65(5):1891-1896. https://doi.org/10.1016/j.ces.2009.11.011

Lee SL, Yang JH, 1997. Modeling of Darcy-Forchheimer drag for fluid flow across a bank of circular cylinders. *International Journal of Heat and Mass Transfer*, 40(13):3149-3155. https://doi.org/10.1016/S0017-9310(96)00347-X

Lefebvre LP, Banhart J, Dunand DC, 2008. Porous metals and metallic foams: current status and recent developments. *Advanced Engineering Materials*, 10(9):775-787. https://doi.org/10.1002/adem.200800241

Li T, Li M, Jing XQ, et al., 2019. Influence mechanism of pore-scale anisotropy and pore distribution heterogeneity on permeability of porous media. *Petroleum Exploration and Development*, 46(3):594-604. https://doi.org/10.1016/S1876-3804(19)60039-X

Liu DD, Tran T, 2018. Microfluidic mixing using PDMS-based microporous structures. *Microfluidics and Nanofluidics*, 22(11):123. https://doi.org/10.1007/s10404-018-2142-5

Lock PA, Jing XD, Zimmerman RW, et al., 2002. Predicting the permeability of sandstone from image analysis of pore structure. *Journal of Applied Physics*, 92(10):6311-6319. https://doi.org/10.1063/1.1516271

Loosveldt H, Lafhaj Z, Skoczylas F, 2002. Experimental study of gas and liquid permeability of a mortar. *Cement and Concrete Research*, 32(9):1357-1363. https://doi.org/10.1016/S0008-8846(02)00793-7

Lu T, Tang YM, Tie YB, et al., 2023. Fractal analysis of small-micro pores and estimation of permeability of loess using mercury intrusion porosimetry. *Journal of Zhejiang University-SCIENCE A (Applied Physics & Engineering)*, 24(7):584-595. https://doi.org/10.1631/jzus.A2200528

Lu TJ, Stone HA, Ashby MF, 1998. Heat transfer in open-cell metal foams. *Acta Materialia*, 46(10):3619-3635. https://doi.org/10.1016/S1359-6454(98)00031-7

Mathavan GN, Viraraghavan T, 1992. Coalescence/filtration of an oil-in-water emulsion in a peat bed. *Water Research*, 26(1):91-98. https://doi.org/10.1016/0043-1354(92)90116-L

Miguel AF, 2012. Non-Darcy porous media flow in no-slip

and slip regimes. *Thermal Science*, 16(1):167-176. https://doi.org/10.2298/TSCI100929001M

Nie SK, Liu PF, Ba T, et al., 2023. Seepage experiment and numerical simulation based on microfluidic chip model. *Journal of Zhejiang University (Engineering Science)*, 57(5):967-976 (in Chinese). https://doi.org/10.3785/j.issn.1008-973X.2023.05.013

Pozrikidis C, 1994. The motion of particles in the Hele-Shaw cell. *Journal of Fluid Mechanics*, 261:199-222. https://doi.org/10.1017/S0022112094000315

Raeesi B, Piri M, 2009. The effects of wettability and trapping on relationships between interfacial area, capillary pressure and saturation in porous media: a pore-scale network modeling approach. *Journal of Hydrology*, 376(3-4): 337-352. https://doi.org/10.1016/j.jhydrol.2009.07.060

Santamarina JC, Cho GC, 2004. Soil behavior: the role of particle shape. Advances in Geotechnical Engineering: the Skempton Conference.

Serrenho A, Miguel AF, 2009. Simulation and characterization of high-porosity media for aerosol particle processing: a numerical study. *Journal of Porous Media*, 12(12): 1129-1137. https://doi.org/10.1615/JPorMedia.v12.i12.10

Serrenho A, Miguel AF, 2011. Fluid flow and solid/fluid suspensions flow in 3-D packed beds of spheres: the effect of periodicity of fixed beds. *Defect and Diffusion Forum*, 312-315:871-876. https://doi.org/10.4028/www.scientific.net/DDF.312-315.871

Sharma S, Geyer TF, Arcondoulis EJG, 2023. On the influence of porous coating thickness and permeability on passive flow and noise control of cylinders. *Journal of Sound and Vibration*, 549:117563. https://doi.org/10.1016/j.jsv.2023.117563

Shen JT, Chen SY, 1989. The following behaviours of a spherical particle in fluid flow. *Acta Aerodynamica Sinica*, 7(1): 50-58 (in Chinese).

Straughan B, Harfash AJ, 2013. Instability in Poiseuille flow in a porous medium with slip boundary conditions. *Microfluidics and Nanofluidics*, 15(1):109-115. https://doi.org/10.1007/s10404-012-1131-3

Tamayol A, Bahrami M, 2011a. In-plane gas permeability of proton exchange membrane fuel cell gas diffusion layers. *Journal of Power Sources*, 196(7):3559-3564. https://doi.org/10.1016/j.jpowsour.2010.11.109

Tamayol A, Bahrami M, 2011b. Transverse permeability of fibrous porous media. *Physical Review E*, 83(4):046314. https://doi.org/10.1103/PhysRevE.83.046314

Tamayol A, Bahrami M, 2011c. Water permeation through gas diffusion layers of proton exchange membrane fuel cells. *Journal of Power Sources*, 196(15):6356-6361. https://doi.org/10.1016/j.jpowsour.2011.02.069

Tamayol A, Khosla A, Gray BL, et al., 2012a. Creeping flow through ordered arrays of micro-cylinders embedded in a rectangular minichannel. *International Journal of Heat and Mass Transfer*, 55(15-16):3900-3908. https://doi.org/10.1016/j.ijheatmasstransfer.2012.03.008

Tamayol A, Wong KW, Bahrami M, 2012b. Effects of microstructure on flow properties of fibrous porous media at moderate Reynolds number. *Physical Review E*, 85(2):026318. https://doi.org/10.1103/PhysRevE.85.026318

Tawfik H, Hung Y, Mahajan D, 2007. Metal bipolar plates for PEM fuel cell—a review. *Journal of Power Sources*, 163(2):755-767. https://doi.org/10.1016/j.jpowsour.2006.09.088

von Rickenbach J, Lucci F, Narayanan C, et al., 2014. Multiscale modelling of mass transfer limited heterogeneous reactions in open cell foams. *International Journal of Heat and Mass Transfer*, 75:337-346. https://doi.org/10.1016/j.ijheatmasstransfer.2014.03.060

Wagner A, Eggenweiler E, Weinhardt F, et al., 2021. Permeability estimation of regular porous structures: a benchmark for comparison of methods. *Transport in Porous Media*, 138(1):1-23. https://doi.org/10.1007/s11242-021-01586-2

Wan JM, Wilson JL, 1994. Colloid transport in unsaturated porous media. *Water Resources Research*, 30(4):857-864. https://doi.org/10.1029/93WR03017

Wang P, 2014. Lattice Boltzmann simulation of permeability and tortuosity for flow through dense porous media. *Mathematical Problems in Engineering*, 2014:694350. https://doi.org/10.1155/2014/694350

White FM, 1991. Viscous Fluid Flow. McGraw-Hill, New York, USA.

Yang J, Yin ZY, Laouafa F, et al., 2019. Modeling coupled erosion and filtration of fine particles in granular media. *Acta Geotechnica*, 14(6):1615-1627. https://doi.org/10.1007/s11440-019-00808-8

Yang J, Yin ZY, Laouafa F, et al., 2020a. Hydromechanical modeling of granular soils considering internal erosion. *Canadian Geotechnical Journal*, 57(2):157-172. https://doi.org/10.1139/cgj-2018-0653

Yang J, Yin ZY, Laouafa F, et al., 2020b. Three-dimensional hydromechanical modeling of internal erosion in dike-on-foundation. *International Journal for Numerical and Analytical Methods in Geomechanics*, 44(8):1200-1218. https://doi.org/10.1002/nag.3057

Yang XH, Song SY, Yang C, et al., 2017. Permeability model of micro-metal foam with surface micro-roughness. *Microfluidics and Nanofluidics*, 21(3):32. https://doi.org/10.1007/s10404-017-1863-1

Yang XH, Weldetsadik NT, Hayat Z, et al., 2019. Pressure drop of single phase flow in microchannels and its application in characterizing the apparent rheological property of fluids. *Microfluidics and Nanofluidics*, 23(5):75. https://doi.org/10.1007/s10404-019-2241-y

Yazdchi K, Srivastava S, Luding S, 2011. Microstructural effects on the permeability of periodic fibrous porous media. *International Journal of Multiphase Flow*, 37(8):956-966.

https://doi.org/10.1016/j.ijmultiphaseflow.2011.05.003

Yin ZY, Yang J, Laouafa F, et al., 2023. A framework for coupled hydro-mechanical continuous modelling of gap-graded granular soils subjected to suffusion. *European Journal of Environmental and Civil Engineering*, 27(8): 2678-2699. https://doi.org/10.1080/19648189.2020.1795724

Yovanovich MM, 1974. A general expression for predicting conduction shape factors. The 11th Aerospace Sciences Meeting. https://doi.org/10.2514/6.1973-121

Yu BM, Li JH, 2004. A geometry model for tortuosity of flow path in porous media. *Chinese Physics Letters*, 21(8): 1569-1571. https://doi.org/10.1088/0256-307X/21/8/044

Zhang JF, 2011. Lattice Boltzmann method for microfluidics: models and applications. *Microfluidics and Nanofluidics*, 10(1):1-28. https://doi.org/10.1007/s10404-010-0624-1

Zhang S, Yan H, Teng JD, et al., 2020. A mathematical model of tortuosity in soil considering particle arrangement. *Vadose Zone Journal*, 19(1):e20004. https://doi.org/10.1002/vzj2.20004

Zhou C, Wang WY, Chen KX, et al., 2022. Influence of wettability in immiscible displacements with lattice Boltzmann method. *Journal of Zhejiang University-SCIENCE A (Applied Physics & Engineering)*, 23(9):704-720. https://doi.org/10.1631/jzus.A2200047

Electronic supplementary materials

Sections S1–S4